

An analysis of the FIR/RADIO Continuum Correlation in the Small Magellanic Cloud

Howard Leverenz¹ • Miroslav D. Filipović^{1,2}

Abstract

The local correlation between far-infrared (FIR) emission and radio-continuum (RC) emission for the Small Magellanic Cloud (SMC) is investigated over scales from 3 kpc to 0.01 kpc. Here, we report good FIR/RC correlation down to ~ 15 pc. The reciprocal slope of the FIR/RC emission correlation (RC/FIR) in the SMC is shown to be greatest in the most active star forming regions with a power law slope of ~ 1.14 indicating that the RC emission increases faster than the FIR emission. The slope of the other regions and the SMC are much flatter and in the range of 0.63–0.85. The slopes tend to follow the thermal fractions of the regions which range from 0.5 to 0.95. The thermal fraction of the RC emission alone can provide the expected FIR/RC correlation. The results are consistent with a common source for ultraviolet (UV) photons heating dust and Cosmic Ray electrons (CRe⁻s) diffusing away from the star forming regions. Since the CRe⁻s appear to escape the SMC so readily, the results here may not provide support for coupling between the local gas density and the magnetic field intensity.

Accepted for publication in Astrophysics & Space Science

Keywords galaxies: individual: Small Magellanic Cloud - Magellanic Clouds - infrared: galaxies - radio-continuum: galaxies.

Howard Leverenz

James Cook University, Townsville, QLD 7000, Australia

Miroslav D. Filipović

University of Western Sydney, Locked Bag 1797, Penrith South DC, NSW 1797, Australia

James Cook University, Townsville, QLD 7000, Australia

1 Introduction

One of the most puzzling and robust relationships in extragalactic astronomy is the virtually ubiquitous correlation between far-infrared (FIR) and radio-continuum (RC) measurements of star-forming galaxies (Yun, Reddy, and Condon 2001) (hereafter referred to as Y01). The essentially linear relationship extends for over five orders of magnitude (Condon 1992) exhibiting the amazingly small scatter of ~ 0.2 dex (z dex = 10^z). Virtually all star forming galaxies are included: normal barred and unbarred spiral galaxies, irregular and dwarf galaxies, and Seyferts including radio-quiet quasars. This correlation has been found to apply to galaxies even beyond $z=1$ (Appleton *et al.* 2004).

The standard explanation for these observations is found in models that use the conversion of energy resulting from the formation of young massive stars ($> 20 M_{\odot}$). FIR emission is posited to be the result of dust heated by UV radiation from these massive young stars. These stars also provide energy for the thermal radio emission found in star forming regions. Massive stars quickly evolve to the terminus of their life cycle and explode into supernovae. The supernova remnants (SNRs) expand rapidly into the local interstellar medium (ISM) and the shock wave provides the mechanism for accelerating Cosmic Ray electrons (CRe⁻s) (Helder *et al.* 2009; Schure *et al.* 2009). Those electrons interact with the galactic magnetic field and are thus responsible for the non-thermal (synchrotron) component of the RC emission (Condon 1992). They also interact with particles in the ISM and contribute to the thermal (free-free) component of the RC emission along with UV radiation from hot massive stars.

This simple picture cannot explain the small dispersion in the FIR/RC ratio measured among the diversity

of galaxies which span the observed ranges of star formation rates (SFRs), magnetic field strengths, metallicity, dust grain chemistry, and ISM mass values.

The scale at which models break down provides an important constraint on the physical mechanisms detailed in that model. For galaxy-wide scales some models work well on spiral galaxies. For very small scales, for example, within several kpc of the Sun, the FIR/RC ratios of star forming regions are not consistent with expected FIR/RC values. Instead, the radio emission appears to be primarily thermal (Haslam and Osborne 1987).

Hughes *et al.* (2006) examined the Large Magellanic Cloud (LMC) for 60 μm FIR / 21 cm RC correlations on spatial scales from 1.5 to 0.05 kpc and found a tight correlation on spatial scales above ~ 50 pc.

The SMC can be described as a gas-rich late-type dwarf galaxy (Bolatto *et al.* 2007). It has a gas-to-dust ratio 17 times higher than the Milky Way Galaxy (Koornneef and de Boer 1984). It is a member of the local group and is classified as irregular (ImIV-V) (Sandage *et al.* 1994). It may also be a satellite galaxy of the Milky Way (Westerlund 1997). The SMC is centered at 60.6 ± 3.8 kpc (Hilditch, Howarth, and Harries 2005) from the Galaxy. The spatial scale of the SMC is $0.3\text{pc}''$. The line of sight to the SMC has an extinction of only $AV \sim 0.2$ magnitudes and a reddening of $E(B-V) \sim 0.04$ (Bolatto *et al.* 2007; Schlegel, Finkbeiner, and Davis 1998).

The SMC appears to have been tidally disrupted by a recent close encounter with the LMC (Murai and Fujimoto 1980). There is no trace of any spiral structure in the SMC (Sandage and Tammann 1981) but both a "bar-like" structure and a "wing" have been reported (Westerlund 1997). The bar structure is probably the body of the SMC and contains most of its gas and star formation activity. The wing feature continues into the bridge which is an H I region extending from the SMC to the LMC (Bolatto *et al.* 2007). The SMC may be more complex than the LMC considering that various population centroids vary by $\sim 20'$ in R.A. and by $\sim 1^\circ$ of declination (Westerlund 1997). The SMC has an absolute luminosity of $M_B = 2.9m$ (Westerlund 1997).

The SMC has the lowest metallicity of any gas-rich galaxy in close proximity (Bolatto *et al.* 2007). This makes it one of the best galaxies to provide understanding of processes in very high redshift galaxies. Measurements suggest that the dust grains are mostly silicates rather than carbonaceous grains which distinguish the SMC's ISM from that of the Galaxy (Weingartner and Draine 2001).

The stars resolved in the SMC are blue and red supergiants with $M_B = -7m$. These Population I stars

are accompanied by a resolved region of Population II stars with $M_V = -3m$. Schwering and Israel (1993) identified 249 infrared sources in the SMC. The morphology of the Population II stars has been measured and appears to suggest a spheroidal distribution without the prominent irregular features seen in the younger stars (Bolatto *et al.* 2007; Cioni, Habing, and Israel 2000; Maragoudaki *et al.* 2001; Zaritsky *et al.* 2000). Earlier studies of the motion of H I clouds were interpreted as representing rotation (Westerlund 1997). Recent observations, however, find no evidence for rotation in the SMC (Piatek, Pryor, and Olszewski 2008), (Costa *et al.* 2011).

In this paper, Section 2 discusses the origins and characteristics of the data used in terms of the frequencies of each data set, characteristics of the data, and source instruments. Section 3 discusses the analysis methods applied to the data sets. Section 4 is a discussion of results of the analysis and considers some FIR/RC galaxy models. Data processing and analysis for this paper was done with Miriad (Sault, Teuben, and Wright 1995), Karma (Gooch and Barnes 1996), Matlab (Matlab 2010), DS9 (Joye *et al.* 2003) and Ftools (Blackburn, Payne, and Hayes 1995).

2 Observational Data

The data used for this study are summarized in Table 1. The FIR data are from the IRAS (Miville-Deschênes and Lagache 2005) and the Spitzer satellites (Bolatto *et al.* 2007). The RC data are from the Australian Telescope Compact Array (ATCA) which consists of five movable 22-m antennae, and the Parkes 64m radio telescopes. (For reference see the series of papers on radio-continuum studies of the Magellanic Clouds: Haynes *et al.* (1991); Xu *et al.* (1992); Klein *et al.* (1993); Filipovic *et al.* (1995, 1997, 1998,a,b), Filipovic *et al.* (2002); Payne *et al.* (2004); Filipovic *et al.* (2005); Reid *et al.* (2006); Payne *et al.* (2007), and (Crawford *et al.* 2011; Wong *et al.* 2011,a, 2012)).

Also, included are data sets for H I (Staveley-Smith *et al.* 1997; Stanimirovic *et al.* 1999), H α (Smith, Leiton, and Pizarro), and CO (Mizuno *et al.* 2001) detailed below. In order to make comparisons between the data sets, all of the data are regridded to a common pixel size of $5''$ using a gnomonic projection centered at 15° RA and -73° DEC (equatorial J2000 coordinates). The whole SMC is defined as the data shown in Figure 1. The irregular coverage of the SMC by the Spitzer data suggested that a division of the data sets into several regions would be appropriate. The 160 μm Spitzer data is used as an approximate template for the division into the five

regions. Figure 1 shows the regional definitions superimposed on all of the data sets as defined by the $160\ \mu\text{m}$ Spitzer data. It is clear that the bar of the SMC is represented by regions 1-3 and the wing by regions 4 and 5. Table 2 lists the coordinates of the boundaries and centers of the regions as well as their areas. Table 3 contains the flux densities from each region and from the whole SMC.

2.1 Infrared Data

The IRAS data used in this paper are the improved reprocessed data from the IRAS satellite survey (Miville-Deschênes and Lagache 2005). The data are in two bands: $60\ \mu\text{m}$ and $100\ \mu\text{m}$ and have been corrected for zodiacal light, calibration, zero levels and striping problems (see Figure 1).

The data used from the Spitzer satellite are from the MIPS instrument. They are from the Spitzer Survey of the SMC (S3MC) covering most of the bar and wing (Bolatto *et al.* 2007) in two bands, $70\ \mu\text{m}$ and $160\ \mu\text{m}$. The data are corrected for zodiacal light, Galactic foreground and Cosmic Infrared background using Leroy's published data (Leroy *et al.* 2007) to adjust the final calibration.

2.2 Radio-Continuum Data

Data from two radio telescopes are used in this study; the Parkes Radio Telescope and the Australian Telescope Compact Array (ATCA). For high-resolution correlation investigations, the combined ATCA+Parkes data is used and for the low resolution thermal fraction investigations, the Parkes data from Filipovic *et al.* (1997) is used exclusively due to its superior overall flux-density accuracy.

The high resolution RC data at 21 cm and 13 cm are from observations made with the ATCA telescope in 1992 from October 6th to the 8th. The observations were made using five antennae in the 375 m east-west array configuration (Wong *et al.* 2012; Filipovic *et al.* 2005) at 1.42 GHz and at 2.37 GHz. The angular resolution is $\sim 98''$ (FWHM) and $\sim 40''$ (FWHM). There were 320 pointings used to create a mosaic of data covering an area of $(\sim 20^\circ)^2$. The "short spacing" low spatial frequency data fill is accomplished using Parkes survey data (Filipovic *et al.* 1997).

The 6 cm and 3 cm high resolution continuum data are from (Dickel *et al.* 2010), at 4.8 GHz and 8.6 GHz, using the EW352 (February 2005) and EW367 (February and March 2006) configurations in 3564 individual pointing positions achieving resolutions of $35''$ and $22''$ respectively. The data were reprocessed to include data from a sixth antenna approximately 6 km

from the center of the ATCA as well as including the low spatial frequency data from the Parkes survey (Haynes *et al.* 1991). The addition of this incomplete, $2''$ - $3''$ interference pattern, provides greater resolution to the image for the evaluation of previously unresolved sources and will be used here to enhance morphological studies using wavelet cross correlations. The additional data does not cover the full extent of the SMC but covers all of the area studied in this paper. See Haynes *et al.* (1991); Xu *et al.* (1992); Klein *et al.* (1993); Filipovic *et al.* (1995, 1997, 1998,a,b), Filipovic *et al.* (2002); Payne *et al.* (2004); Filipovic *et al.* (2005); Reid *et al.* (2006); Payne *et al.* (2007), and Crawford *et al.* (2011); Wong *et al.* (2011,a, 2012).

2.3 H I Data

The H I 21 cm data are from observations made with the ATCA telescope in 1992 from October 6th to the 14th and August 2nd and 3rd. The observations were made using five antennas in the 375 m east-west array configuration (Staveley-Smith *et al.* 1995, 1997) at 1.42 GHz. The angular resolution is $\sim 90''$ (FWHM). There were 320 pointings used to create a mosaic of data covering an area of $(\sim 20^\circ)^2$. The "short spacing" low spatial frequency data fill is accomplished using Parkes survey data (Stanimirovic *et al.* 1999) from 1996 March 14th to 17th.

The column densities are corrected for self-absorption using the correction factors from Stanimirovic *et al.* (1999). The H I mass is calculated for each region and the whole SMC and is shown in Table 3. Results reported here of $2.8 \cdot 10^8\ \text{HI}\ M_\odot$ from a $3^\circ \times 3^\circ$ reduced data set compare favorably to a published value of $3.8 \cdot 10^8\ \text{HI}\ M_\odot$ from Stanimirovic *et al.* (1999) for a $5^\circ \times 5^\circ$ image.

2.4 H α Data

The H α data is from the Magellanic Cloud Emission Line Survey (MCELS) program using the UM/CTIO Curtis Schmidt telescope (Smith, Leiton, and Pizarro). The central $3.5^\circ \times 4.5^\circ$ of the SMC are imaged in overlapping $1^\circ \times 1^\circ$ fields with 2048^2 pixels per field in such a way as to provide at least two samples of each pixel. The H α filter is centered on 500.7 nm with a width of 3 nm. Two continuum channels are also imaged, 685 nm, $\delta = 9.5\ \text{nm}$, and 513 nm, $\delta = 3\ \text{nm}$ for stellar contribution subtraction.

2.5 $^{12}\text{CO}\ j = (1 - 0)$ Data (115.271 GHz)

CO data is from the NANTEN sub-millimeter observatory on Pampa la Bola in the Atacama Desert, Chile

Table 1 Data used in this study include IRAS and Spitzer satellite images, Radio images from ATCA and Parkes telescopes, H I images, H α images from NFCCD/CTIO and CO $j = (1 - 0)$ images.

Band	Telescope	Resolution (arcsec)	Resolution (pc)	Reference
60 μm	IRAS	120	35.3	(Miville-Deschnes and Lagache 2005)
100 μm	IRAS	120	35.3	(Miville-Deschnes and Lagache 2005)
70 μm	Spitzer	18	5.3	(Bolatto <i>et al.</i> 2007)
160 μm	Spitzer	40	11.8	(Bolatto <i>et al.</i> 2007)
3 cm RC	ATCA+Parkes	2	0.6	(Dickel <i>et al.</i> 2010) a
6 cm RC	ATCA+Parkes	3	0.9	(Dickel <i>et al.</i> 2010) a
6 cm RC	Parkes	162	48.6	(Filipovic <i>et al.</i> 1997) a
13 cm RC	ATCA+Parkes	60	17.6	(Staveley-Smith <i>et al.</i> 1997; Stanimirovic <i>et al.</i> 1999) a
21 cm RC	ATCA+Parkes	90	26.4	(Staveley-Smith <i>et al.</i> 1997; Filipovic <i>et al.</i> 1997) a
21 cm RC	Parkes	1128	338	(Filipovic <i>et al.</i> 1997) a
H I	ATCA+Parkes	98	28.8	(Staveley-Smith <i>et al.</i> 1997; Stanimirovic <i>et al.</i> 1999) a
H α	NFCCD/CTIO	3	0.9	(Smith, Leiton, and Pizarro)
CO	NANTEN 4-m	156	45.8	(Mizuno <i>et al.</i> 2001)

^aAlso see Haynes *et al.* (1991); Xu *et al.* (1992); Klein *et al.* (1993); Filipovic *et al.* (1995, 1997, 1998,a,b), Filipovic *et al.* (2002); Payne *et al.* (2004); Filipovic *et al.* (2005); Reid *et al.* (2006); Payne *et al.* (2007), and Crawford *et al.* (2011); Wong *et al.* (2011,a, 2012)

Table 2 Coordinates in degrees of the boundaries of the 5 regions as shown in Figure 1. Each region is defined by the coordinates of the region’s vertices. The centers of each region and the areas are also shown.

Vertex	SE	SW	NW	NE	Center	Area
Regions	RA/DEC	RA/DEC	RA/DEC	RA/DEC	RA/Dec	Deg ²
1	12.9528/-73.8571	10.4595/-73.5514	11.7169/-72.7425	14.0390/-73.0425	12.2920/-73.2984	0.6647
2	15.0297/-73.1336	12.4418/-72.8108	13.3596/-72.1624	15.8403/-72.4741	14.1679/-72.6452	0.5767
3	16.5846/-72.5451	14.0808/-72.2471	14.8865/-71.6050	17.3130/-71.8711	15.7163/-72.0671	0.5679
4	19.4525/-73.7627	16.6597/-73.5182	17.6519/-72.6450	20.2119/-72.8758	18.4940/-73.2004	0.7432
5	16.8303/-73.3567	15.2447/-73.1735	16.0482/-72.4953	17.6098/-72.6634	16.4332/-72.9222	0.3589
SMC	20.5906/-74.4285	9.4094/-74.4285	10.2887/-71.4425	19.7253/-71.4424	15.0000/-73.0000	9.0000

Table 3 Regional measured data and derived results for H I in terms of M_{\odot} and H_2 mass from CO measurements. The percentages refer to the portion of the total summed over all regions for each wavelength shown in this table. The SMC data refers to the whole SMC data set which includes data not contained in the regions.

Data	Region 1	Region 2	Region 3	Region 4	Region 5	SMC	Units
60 μm	24.9(39%)	13.1(20%)	16.0(25%)	7.33(11%)	2.88(4%)	92.6	10^2 Jy
100 μm	47.6(37%)	26.4(21%)	29.3(23%)	17.7(14%)	7.47(6%)	208.	10^2 Jy
70 μm	26.6(34%)	18.8(24%)	17.0(22%)	9.02(12%)	5.98(8%)	102.	10^2 Jy
160 μm	73.9(35%)	42.2(20%)	45.7(22%)	34.3(16%)	15.2(7%)	332.	10^2 Jy
H I	2.64(30%)	1.87(22%)	1.41(16%)	1.79(21%)	0.954(11%)	48.2	10^{27} H I /cm ²
H I	4.56(30%)	3.23(22%)	2.43(16%)	3.09(21%)	1.65(11%)	27.9	10^7 H I M_{\odot}
H α	44.1(30%)	30.2(20%)	54.7(37%)	15.6(10%)	4.78(3%)	149.	10^{-11} ergs/cm ² /s
CO	494.(52%)	121.(13%)	179.(19%)	150.(16%)	4.72(0%)	82.6	10^2 K km/s
H_2	71.5(50%)	13.9(9.7%)	32.8(23%)	24.6(17%)	0.54(0.4%)	159.	$10^5 M_{\odot}$
3 cm	6.28(26%)	3.80(16%)	7.61(32%)	4.49(19%)	1.57(7%)	54.8	Jy
6 cm	5.80(29%)	3.87(19%)	6.47(32%)	2.91(15%)	0.861(4%)	33.5	Jy
13 cm	7.59(31%)	5.69(23%)	7.63(31%)	2.94(12%)	0.680(3%)	35.1	Jy
21 cm	7.55(29%)	6.46(24%)	7.59(29%)	3.69(14%)	1.17(4%)	40.0	Jy

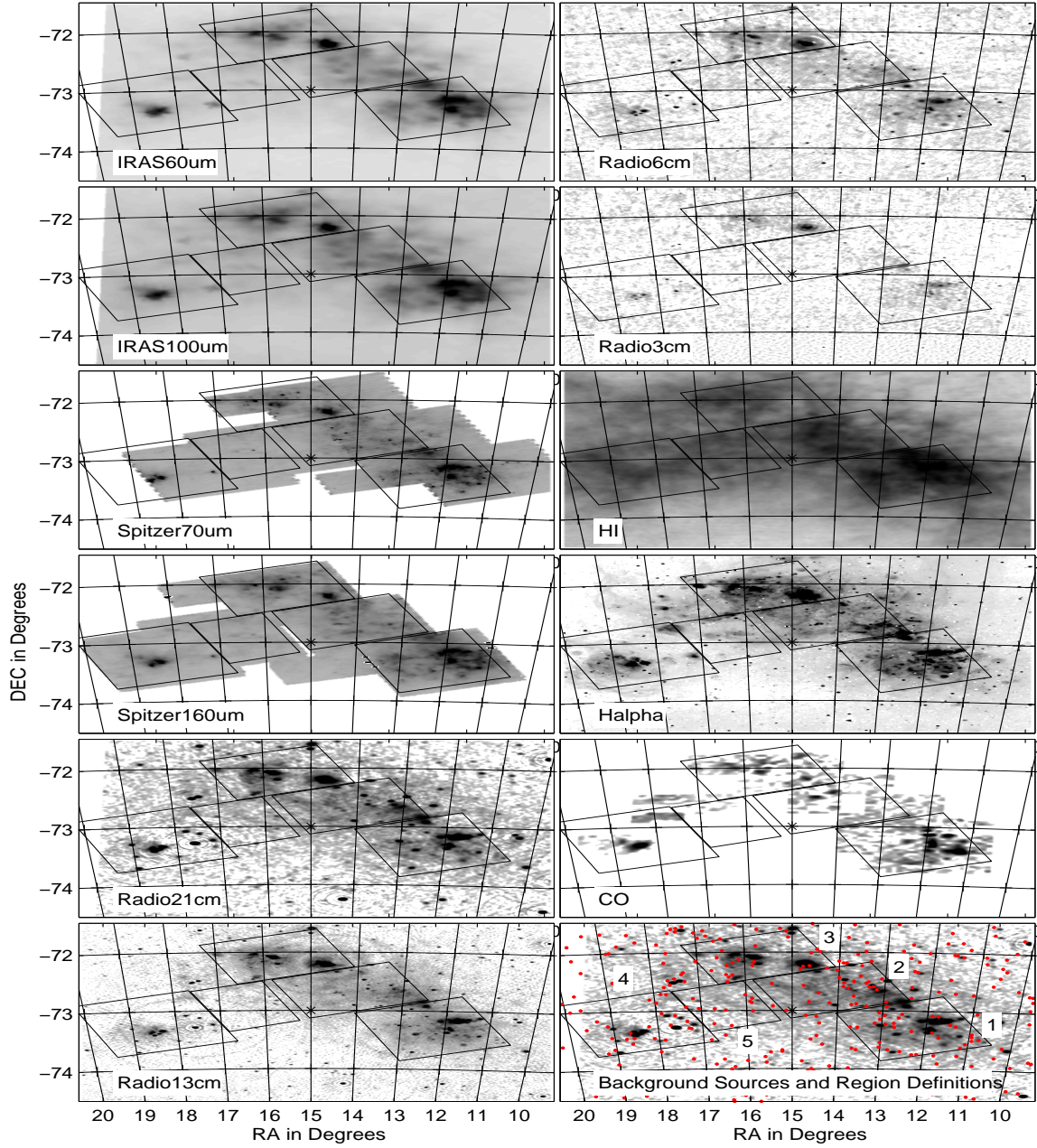


Fig. 1 All of the data sources used in this paper are shown in this figure. The IRAS FIR data are the improved reprocessed data from the IRAS satellite survey (Miville-Deschênes and Lagache 2005). Spitzer FIR data are from the Spitzer Survey of the Small Magellanic Cloud (S3MC) (Bolatto *et al.* 2007). The 160 μm Spitzer data provides the outline for the definition of the 5 regions used in this analysis which is shown in the background source panel. The four sources of RC data used in this paper are shown in this figure. HI data from the ATCA and Parkes telescopes are combined to produce the data used here. Details of the data are found in Table 1. Data are displayed with North to the top and East to the left and J2000 coordinates in degrees. These plots are smoothed with a 25'' Gaussian kernel and scaled by the square root of the intensity.

(Mizuno *et al.* 2001). The NANTEN telescope is used at 2.6 mm wavelength and the observations have a resolution of $2.6'$. Regions 1-3 are well covered by this data. Region 4 has coverage primarily around N84 and there is only incidental coverage of Region 5.

The conversion factors for the CO data to H_2 mass used in this paper are from Leroy *et al.* (2011). Leroy calculated 3 different conversion factors for the SMC for different parts of the SMC which varied by 40%. (Leroy's West \rightarrow Region 1; North \rightarrow Region 3; East \rightarrow Region 4; Average of Leroy's West and North \rightarrow Region 2 and Region 5). The results of this conversion is expected to reveal only the most dense H_2 clouds. The conversion factors applied to the 5 regions and the overall average value applied to the entire SMC are shown in Table 4.

2.6 Background sources

Since the SMC is essentially transparent to 1.42 GHz RC radiation and it presents a cross section of several deg^2 , many background sources are expected to be visible in the SMC RC data. These background sources were catalogued by Payne *et al.* (2004) Crawford *et al.* (2011); Wong *et al.* (2011,a, 2012). This data consist of 717 RC sources of which 616 were identified as background sources. They are plotted in Figure 1 along with the numbers assigned to each of the five regions on an image of the 21 cm RC data.

3 Analysis

The analysis presented here uses cross correlations between several different wavelengths using traditional pixel-by-pixel correlations as well as wavelet correlations. The pixel-by-pixel correlation studies provide intensity correlations as a function of position. The wavelet cross correlation technique probes morphological correlations which are sensitive to changes over a range of spatial scales. FIR/RC correlation is studied

over the entire SMC as well as the regions defined previously.

All of the correlation analysis with RC data is done excluding data at the coordinates of the background sources. The mask consisted of Gaussian function with a FWHM of $2'$ applied to the coordinates of each background source. The data sets also had a median filter of $15'' \times 15''$ applied to remove zero pixels and provide a slight smoothing.

3.1 SMC and Regional FIR/RC ratios

An examination of the FIR/RC correlation in the SMC compared to measurements from more distant galaxies is shown in Figure 2. This correlation is measured down to scale factors of less than 1 kpc by considering each of the five regions in the SMC (see Figure 1). Three of these regions cover the bar structure and two cover the portion of the wing structure that is closest to the bar. The structure of the correlations within the regions is shown in images which display the organization of the FIR and RC emissions giving rise to the measured values.

Using the $60 \mu\text{m}$ IRAS IR flux and the 21 cm RC flux, a FIR/RC calculation is made for each of the five SMC regions and the whole SMC (defined as a $3^\circ \times 3^\circ$ region centered at RA 15° Dec -73°). These results are directly compared to the survey done by Y01. Y01's catalog identified radio counterparts to the IRAS Redshift Survey galaxies with $60 \mu\text{m}$ IR fluxes of $\gtrsim 2 Jy$. The catalog includes 1750 galaxies and contains radio positions and redshifts. Also tabulated are 1.4 GHz radio fluxes from the selected galaxies and their IRAS fluxes.

An ordinary linear least squares fit is performed on this data to determine the FIR/RC ratio as defined by the data from Y01. The fit equation calculated in this paper is Equation 1:

$$\log(L_{1.4\text{GHz}}) = \left(\frac{0.995W}{Hz}\right) \cdot \log\left(\frac{L_{60\mu\text{m}}}{L_\odot}\right) + \left(\frac{12.377W}{Hz}\right) \quad (1)$$

Table 4 CO conversion factors to H_2 from Leroy *et al.* (2011) as assigned to the SMC regions and the calculated H_2 mass for each region.

Region	Conversion Factor $M_\odot pc^{-2} (K km s^{-1})^{-1}$	H_2 $*10^5 M_\odot$
1	67	71.5
2	53	13.9
3	85	32.8
4	67	24.6
5	53	0.54
SMC	69	159

For each $5'' \times 5''$ pixel of the SMC data sets, the value of the FIR/RC ratio is calculated. The sums of this ratio for each region is plotted on the graph with Y01's data set (Figure 2). The line described by the fit equation is extended through the SMC data sets presented in this paper to show how the fitted ratio of the Y01 data corresponds with this SMC data. The correlation is evident in all five regions and for the whole SMC. The distance from Y01's regression fit line to

the regional and complete SMC data are very small: from $\Delta=0.017$ dex to $\Delta=0.115$ dex. These differences changed slightly depending on whether the background sources are included or not. The differences for each region and the whole SMC are shown in Table 5 including the change due to background sources.

For comparison, Figure 2 also plots the LMC correlation calculated from data published on the LMC by Hughes *et al.* (2006). The distance to Y01's regression line for the LMC is calculated here to be $\Delta=0.308$ dex.

3.2 Pixel by Pixel analysis

Pearson's linear correlation coefficient calculation is performed between several pairs of data sets, Equation 2. For each pair of data sets, the data set with the smallest FWHM beamwidth is convolved with a Gaussian kernel to smooth it to the same FWHM as the lower resolution data. The sampling is then done at a spacing corresponding to the beamwidth of the lower resolution data to guarantee statistical independence of the samples. In this equation f_N refers to the N^{th} image, f_{Ni} refers to the i^{th} pixel of the N^{th} image and r_p is the Pearson's linear correlation coefficient.

$$r_p = \frac{\sum (f_{1i} - \langle f_1 \rangle) (f_{2i} - \langle f_2 \rangle)}{\sqrt{\sum (f_{1i} - \langle f_1 \rangle)^2 \sum (f_{2i} - \langle f_2 \rangle)^2}} \quad (2)$$

The error in this correlation is calculated as follows:

$$\Delta r_p = \frac{\sqrt{1 - r_p^2}}{\sqrt{n^2 - 2}} \quad (3)$$

The formal errors for these data sets are $\simeq 10\%$ since n , the total number of points in a data set, is $\sim 10^3$ when the resolution of the data sets are considered. Of course, the real error is possibly larger due to calibration errors and other systematic errors in the data.

Table 5 Comparison of the difference between the data fit to data from Yun (Yun, Reddy, and Condon 2001) and the current measurements. The contribution to the fit from the background sources is shown to contribute less than 10 percent to the fit discrepancy.

Regions	Without BKG dex	With BKG dex	Difference %
1	0.1159	0.1153	-0.52
2	0.0431	0.0433	0.46
3	0.0465	0.0460	-1.08
4	0.0183	0.0172	-6.39
5	0.0297	0.0283	-4.94
SMC	0.0783	0.0783	0.00

Perfectly correlated images would have a coefficient of 1 and perfectly anti-correlated images would have a coefficient of -1. Table 6 shows various pairs of data sets for the 5 regions and the correlations therein. Values above 0.7 or 0.8 in Table 6 indicates moderate to strong correlation. Those values are printed in bold face type.

Region 1 and Region 5 have the highest correlations with the FIR-H I data sets and includes N 19 and NGC 267. SMC SNR position data from Filipovic *et al.* (2005) is used to determine the SNR population of each region. Region 1 has the largest concentration of H I for the SMC (see Table 3) and a complex of 5 SNRs around SNR B0045-734. There are 4 other SNRs in Region 1. Region 5 contains no identified SNRs. Region 2 shows very little correlation in any of the data set pairs. There are two identified SNRs in Region 2. Region 3 is dominated by the H II region N 66 and NGC 346, and shows good correlations in the FIR-RC data sets as well as the H α correlations with the RC and FIR data. Region 3 contains 12 SNRs. Region 4 shows moderate to strong correlations of the IR-CO data sets for the coolest dust. Region 4 is not well covered by the 70 μm or the CO data. There are no known SNRs in Region 4. It does, however, contain NGC 456.

Figure 3 shows the scatter plots of the 21 cm continuum and 60 μm IR data for the pixels of all five regions and the whole SMC. For each pair of data sets, the data set with the smallest FWHM beamwidth is convolved with a Gaussian kernel to smooth it to the same FWHM as the lower resolution data. The sampling is then done at a spacing corresponding to the beamwidth of the lower resolution data to guarantee statistical independence. It also shows two different Least Squares Fits to each data set. The blue line is the Ordinary Least Squares Fit, OLS and the green line is the Weighted Least Squares Fit (WLS) calculated using the Matlab function *lscov* (Matlab 2010). The OLS assumes the error of each data point is the same and consequently weights every data point equally. The WLS uses a weighting for each data point which here is calculated as the square root of the sum of the squares of the values of each axis linearly weighted from 0.01 to 1 scaled to the value of the data point from the minimum value to the maximum value of each data set.

The difference in the slope and offset of these fit lines and the averages are shown in Table 7. The last row contains the differences in percent of the OLS slope and the WLS slope of the fitted lines. It is expected that the OLS fit would be a better representation of the entire data set whereas the WLS fit is weighted to lower the contribution of data with larger calculated errors and would describe the strongest data without the effect of outlier points.

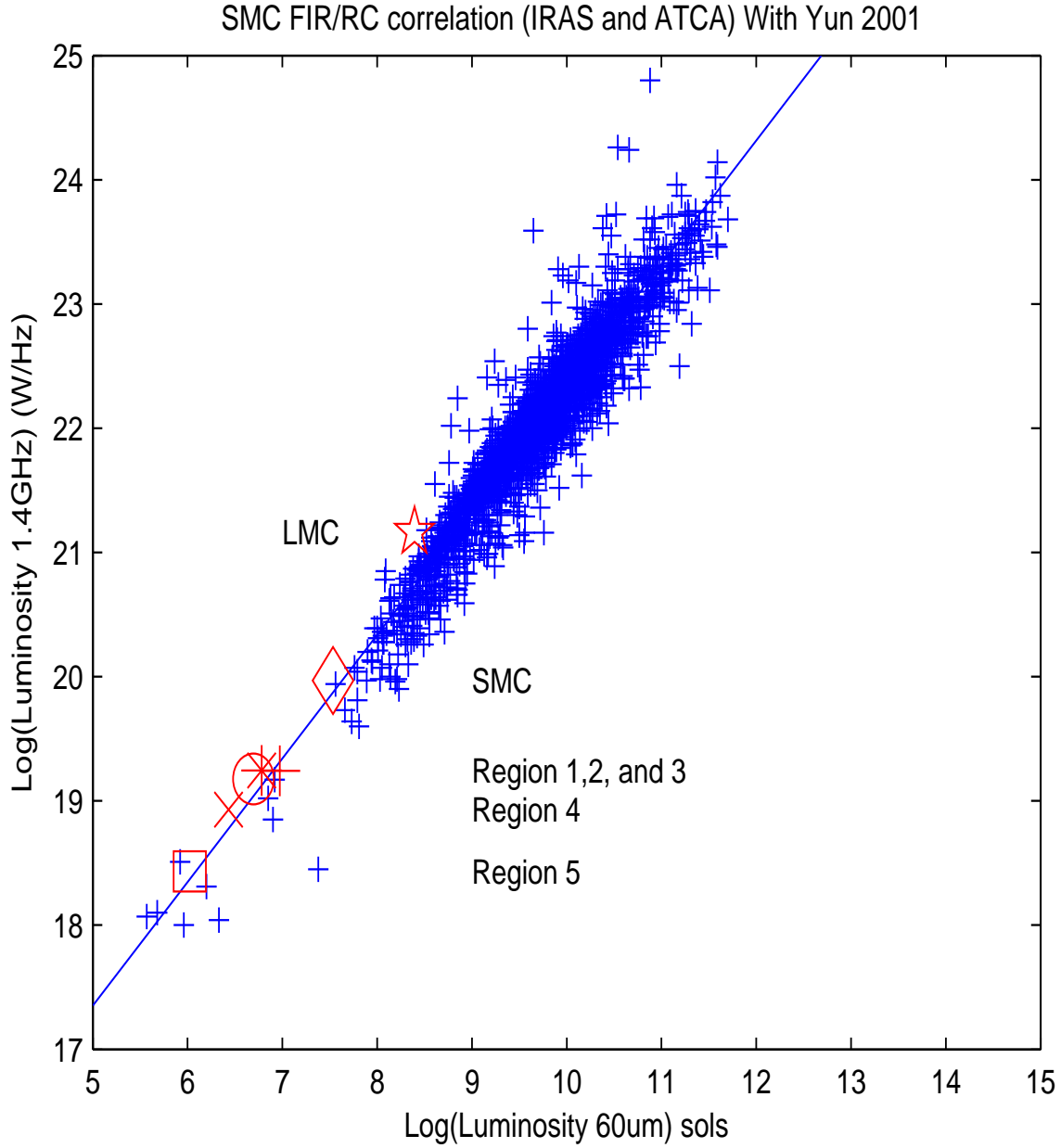


Fig. 2 FIR/RC correlations for the whole SMC (defined as a $2.5^\circ \times 2.5^\circ$ region centered at RA 15° Dec -73°) and the regions defined in this paper compared to the data from Yun, Reddy, and Condon (2001). Regions 1-5 and whole SMC are plotted and labeled. (1-plus, 2-circle, 3-asterisk, 4-x, 5-square, and SMC-diamond). Additionally, the correlation calculated from data published on the LMC by Hughes *et al.* (2006) is plotted using the star marker.

Table 6 Pearson correlations for pairs of data sets. All results have a calculated error of $\simeq 10\%$. For each pair of data sets, the data set with the smallest FWHM beamwidth is convolved with a Gaussian kernel to smooth it to the same FWHM as the lower resolution data. The sampling is then done at a spacing corresponding to the beamwidth of the lower resolution data. Values above 0.7 are emphasized as having good correlation.

Data Sets	Regions				
	1	2	3	4	5
RC 21 cm					
60 μm	0.620	0.686	0.825	0.444	0.263
70 μm	0.573	0.513	0.585	0.484	0.193
100 μm	0.574	0.607	0.752	0.410	0.201
160 μm	0.587	0.458	0.656	0.515	0.168
RC 13 cm					
60 μm	0.609	0.700	0.815	0.501	0.304
70 μm	0.610	0.628	0.752	0.720	0.127
100 μm	0.569	0.638	0.740	0.461	0.244
160 μm	0.629	0.577	0.661	0.616	0.129
CO					
RC 21 cm	0.272	0.059	0.311	0.422	-0.255
RC 13 cm	0.296	0.073	0.305	0.347	0.032
60 μm	0.531	0.130	0.318	0.759	0.116
70 μm	0.531	0.142	0.405	0.471	0.190
100 μm	0.554	0.170	0.378	0.769	0.146
160 μm	0.599	0.168	0.479	0.896	0.181
H I	0.304	0.205	0.173	0.444	0.293
H α	0.312	0.018	0.307	0.291	-0.055
H I					
RC 21 cm	0.404	0.255	0.059	0.092	0.137
RC 13 cm	0.443	0.307	0.044	0.137	0.109
60 μm	0.762	0.584	0.197	0.394	0.748
70 μm	0.709	0.545	0.209	0.226	0.790
100 μm	0.810	0.680	0.338	0.472	0.833
160 μm	0.773	0.708	0.401	0.506	0.857
H α					
RC 21 cm	0.377	0.659	0.859	0.563	0.329
RC 13 cm	0.273	0.597	0.830	0.722	0.237
60 μm	0.205	0.327	0.816	0.516	0.408
70 μm	0.387	0.290	0.638	0.535	0.018
100 μm	0.158	0.297	0.731	0.475	0.350
160 μm	0.438	0.247	0.661	0.179	0.020

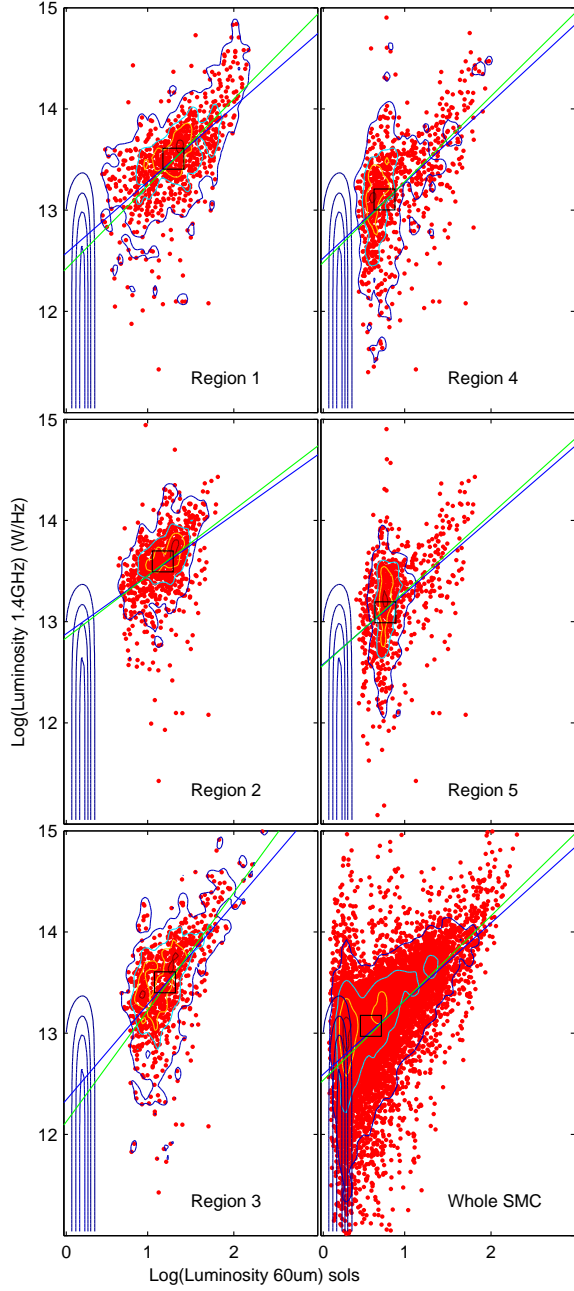


Fig. 3 Scatter plot of the regions and the whole SMC. For each pair of data sets, the data set with the smallest FWHM beamwidth is convolved with a Gaussian kernel to smooth it to the same FWHM as the lower resolution data. The sampling is then done at a spacing corresponding to the beamwidth of the lower resolution data. The two lines in each plot are the ordinary least squares and weighted least squares fits to the data. The OLS is in green, the WLS in blue. The contours in the data plot show the density of data points and the Gaussian distribution of the background noise. Those contours are at 5, 30, 60, and 90% of the peak data density. The position of the square is the average of the data set.

Strong to moderate Pearson correlations in FIR-RC, FIR-HI, and IR-H α in Regions 1 and 3 seen in Table 6 appear to show the effect of two populations of data in those regions. The range of OLS slopes in the regions is 0.594 to 0.978 while the WLS slopes range from 0.638 to 1.144 over the regions. In every region the OLS slope is flatter than the WLS slope. The set of contour lines to the left of the figures is from the background noise using measurements from the north east corner of the whole SMC data set which are not considered to be part of the SMC. The measured average value and the RMS noise are used to calculate a background Gaussian noise distribution and the results of this distribution are used to create the noise contours for the background. Also shown are four contours which are created by binning the luminosity data into a 100×100 bin array. The contours shown are at 5, 30, 60 and 90% of the maximum bin count. Visually examining these contours indicates that 90% of the data is found with values quite symmetric to the fitted lines, both OLS and WLS. This suggests that the WLS is a better representative of the data in the regions. The Gaussian noise distribution calculated for the measured background noise uses the same scaling. It is clear that there is not a significant contribution by noise to the scatter plot for any of the five regions. However, the whole SMC plot includes portions of sky which are not part of the SMC and contain only noise so that there is considerable overlap seen in the lower luminosity values of the scatter plot with the noise contours. The plotted square in each data set is the location of the average pixel value.

3.3 SMC FIR/RC ratio map

In order to relate particular physical structures in the SMC with variations in the FIR/RC ratio, Figure 4 is calculated showing the log ratio of FIR and 21 cm RC data. The q value map is calculated using the formula from Helou *et al.* (1988) with the IRAS $60 \mu m$ and $100 \mu m$ data sets. The FIR value is calculated in equation 4.

$$\left(\frac{FIR}{Wm^{-2}} \right) = 1.26 \cdot 10^{-14} \left(\frac{2.58S_{60\mu m} + S_{100\mu m}}{Jy} \right) \quad (4)$$

The q values of the pixels are calculated with Equation 5.

$$q = \log \left(\frac{FIR}{3.75 \cdot 10^{12} Wm^{-2}} \right) - \log \left(\frac{S_{RC}}{Wm^{-2} Hz^{-1}} \right) \quad (5)$$

The average value of the ratio is $q=2.65$. This suggests that the SMC has a slight FIR excess when compared to Y01's average figure of $q=2.34$. Approximately

Table 7 For each pair of data sets, the data set with the smallest FWHM beamwidth is convolved with a Gaussian kernel to smooth it to the same FWHM as the lower resolution data. The sampling is then done at a spacing corresponding to the beamwidth of the lower resolution data. Data set averages for RC 21 cm, Log(Luminosity 1.4 GHz)(W/Hz), and FIR, Log(luminosity $60 \mu m$) sols, and fit parameters to $y=ax + b$ using Ordinary Least Squares fit, OLS, and Weighted Least Squares fit, WLS. These numerical values are shown graphically in Figure 3. The differences in slope values are also shown with the WLS always larger than the OLS value. For comparison, Y01's data as fitted here using OLS gives $a = 0.995$ and $b = 12.38$.

	Regions					
	1	2	3	4	5	SMC
RC	13.51	13.60	13.50	13.11	13.10	13.07
FIR	1.296	1.169	1.195	0.753	0.762	0.590
OLS a	0.730	0.594	0.978	0.776	0.725	0.755
WLS a	0.846	0.638	1.144	0.829	0.752	0.819
OLS b	12.55	12.86	12.31	12.50	12.56	12.57
WLS b	12.40	12.82	12.09	12.46	12.55	12.51
$\Delta a\%$	13.7	6.8	14.5	6.4	3.6	7.8

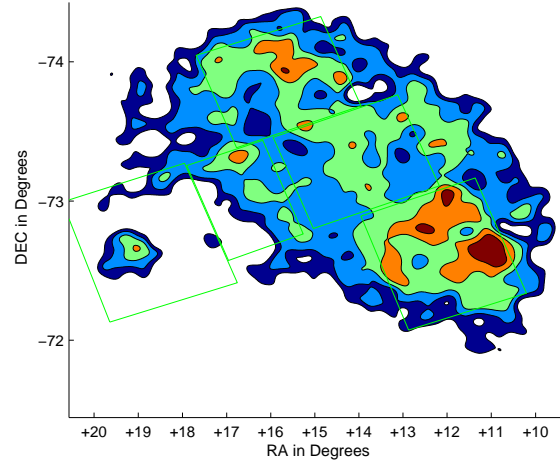


Fig. 4 This figure shows the q value plot of the SMC which has been convolved with a Gaussian kernel of 108 pc FWHM. Red > 2.95 > yellow > 2.75 > green > 2.55 > light blue > 2.35 > dark blue > 2.15 > white.

98% of Y01's galaxies are within a factor of 5 of 2.65, ~ 1.6 to ~ 3.0 . Figure 4 shows the distribution of q values across the SMC from $q < 2.15$ to $q > 2.95$.

Region 1, with an average q of 2.80, has a large portion of its area with $q \geq 2.65$. This suggests that there is abundant dust in the area. Relatively high Pearson correlations of FIR with H I are also seen in Table 6 for Region 1. There are 9 SNRs in this region. The strongest RC feature in this region is N 19 containing SNR B0045-734 (Payne *et al.* 2004) (Crawford *et al.* 2011; Wong *et al.* 2011,a, 2012). The other regions have extended areas where the RC excess is present.

Region 2, with an average q of 2.58, has a large portion of its area with $q \leq 2.65$. With two SNRs in this region, it could be inferred that there is not much star-forming activity in this region so that the dust is cooler.

Region 3, with an average q of 2.70, has 12 SNRs with similar areas with $q < 2.65$ and $q > 2.65$. The high star formation rate leads to the very high Pearson correlation seen in all of the IR data maps with the 21 cm data. $H\alpha$ correlates also very well with the RC data and the FIR data.

Region 4, with an average q of 2.75, is dominated by background radio source SMC B0109-7330. It has a portion of its area with significant dust and gas in the eastern part of the region. It is the only region that has strong correlation of CO with the IR emission in the Pearson correlation results.

Region 5, with q of 2.73, has very small total energy emission, 0.2 – 0.3 of the average of the other 5 regions. Scaled for area, it is ~ 0.4 - ~ 0.6 of the average.

3.4 Wavelet analysis

Wavelets can be used as a tool for scaling analysis (Frick *et al.* 2001). It is a technique that convolves the data with a family of self-similar analyzing functions that depend on scale and location. The family of analyzing functions is defined by dilations and translations of the analyzing function, also called the mother function. In two dimensions, the continuous wavelet transformation can be written as follows:

$$W(a, \vec{x}) = \frac{1}{a^\kappa} \int_{-\infty}^{\infty} \int_{-\infty}^{\infty} f(\vec{x}') \Psi^* \left(\frac{\vec{x}' - \vec{x}}{a} \right) d\vec{x}' \quad (6)$$

In this expression, $\vec{x} = (x, y)$ and $f(\vec{x})$ is the two dimensional data set for which the Fourier transform exists, $\Psi^*(\vec{x})$ is the complex conjugate of the analyzing function, a is the scale factor, and κ is the normalizing parameter.

The analyzing function used here is the Pet Hat (PH) function (Frick *et al.* 2001). This function is defined in terms of its Fourier transform as follows:

$$\hat{\Psi}(\vec{k}) = \cos^2 \left(\frac{\pi}{2} \log_2 \frac{k}{2\pi} \right) : \pi < |\vec{k}| < 4\pi \\ = 0 : \text{otherwise} \quad (7)$$

This function specifies an annulus in Fourier space with a median radius of 2π and is non-zero only for the specified annulus.

3.5 Wavelet cross correlation

Given a two dimensional data set, the energy of the transformation as a function of scale factor a over the entire plane is:

$$M(a) = \int_{-\infty}^{\infty} \int_{-\infty}^{\infty} |W(a, \vec{x})|^2 d\vec{x} \quad (8)$$

The wavelet cross correlation coefficient as a function of a is calculated as follows:

$$r_w(a) = \frac{\iint W_1(a, \vec{x}) W_2^*(a, \vec{x}) d\vec{x}}{\sqrt{[M_1(a) M_2(a)]}} \quad (9)$$

where the subscripts refer to the source data sets used in the cross correlation.

The error in the cross correlation is calculated as follows:

$$\Delta r_w(a) = \frac{\sqrt{1 - r_w^2(a)}}{\sqrt{\left(\frac{L}{a}\right)^2 - 2}} \quad (10)$$

where L is the linear size of the data set. For the data used here $\Delta r_w(a)$ is $\lesssim 15\%$.

For each pair of data sets used in wavelet cross correlation, the data set with the smallest FWHM beamwidth is convolved with a Gaussian kernel to smooth it to the same FWHM as the lower resolution data. The sampling is then done at a spacing corresponding to the beamwidth of the lower resolution data. Figure 5 shows wavelet correlations of several data sets with the 21 cm RC in all 5 regions. The smallest scale that can be used to analyze the data is the resolution of the data. The largest scale is dependent on the overall size of the data set. The smallest linear dimension of the data set should be no less than four times the largest scale factor used in the analysis. The resolution of the 21 cm data is $90''$ (27 pc) and the finest resolution calculated is $80''$ (24 pc). The correlation is performed with IRAS 60 μm and 100 μm data with $120''$

(36 pc) resolution, Spitzer 70 μm and 160 μm data with 18'' (5.4 pc) and 40'' (12 pc) resolution respectively, H I data with 98'' (30 pc) resolution, $H\alpha$ with 3'' (1 pc) resolution, and CO data with 156'' (46 pc) resolution. For the data sets used here, the maximum valid scale value for the wavelet cross correlation is 794'' (238 pc) for Regions 1-4 and 501'' (150 pc) for Region 5 except for the CO data.

The CO map is much more irregular than the other data sets. Region 1 is close to being fully covered with the cross correlation results beginning at 125''. Region 2 is not well covered and has a large hole in the coverage in the center of that region. The only scale factors that satisfy validity requirements are at 125'' and 200'', both of which are shown. Region 3 is also close to being fully covered with the cross correlation results beginning at 125''. Region 4 is split into two smaller areas. Interpreting the wavelet cross correlation in the region is problematic. Region 5 is just a sliver of data that is too small and irregular to use in a wavelet correlation. Wavelet correlations of Regions 4 and 5 are not calculated.

3.6 Wavelet cross correlation for FIR with RC

Table 8 shows the smallest scale factors for which excellent wavelet cross correlation is measured. Frick *et al.* (2001) regarded 0.75 or above as representing an excellent correlation between images and will be referred to here as the correlation threshold. The scale factors are extracted from the data shown in Figure 5. The data clearly shows strong morphological correlations of dust emission in the FIR with the 21 cm continuous emission from the defined regions of the SMC down to beamwidth limited minimum scale factor, ~ 35 pc. In Regions 2 and 3, the limit of the correlations is primarily due to the data resolution. Table 9 shows the

Table 8 21 cm RC wavelet cross correlation scale factors in pc for Region 1 through 5 with data from several other data sets. Listed are the minimum scale factors in pc for which the wavelet cross correlations are considered excellent, which is taken to be ≥ 0.75 . Note that the **BoldFace** values are limited by the beamwidth of one of the data sets.

	Regions				
	1	2	3	4	5
IRAS 60 μm	53.2	35.3	35.3	51.5	129.8
IRAS 100 μm	57.3	35.3	35.3	55.9	136.1
Spitzer 70 μm	52.4	28.3	24.0	50.6	50.3
Spitzer 160 μm	54.5	33.4	24.0	52.6	53.2
H I	129.8	—	170.1	88.7	83.6
$H\alpha$	30.6	25.3	24.0	45.9	53.2
CO	97.0	—	229.0	—	—

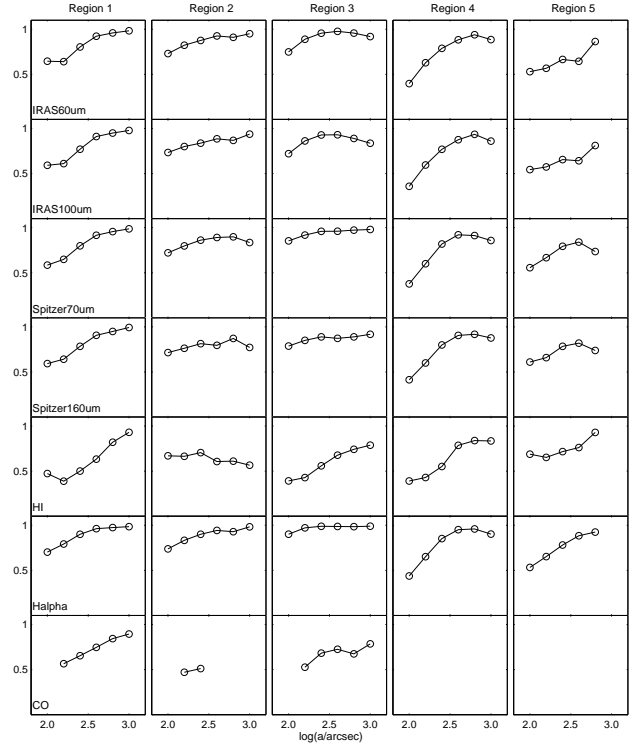


Fig. 5 21 cm RC wavelet cross correlation plots for Region 1 through 5 with data from several other data sets. The data points for Regions 1-4 are calculated at scale factors of 80'', 125'', 200'', 316'', 501'', and 794'' which correspond to 24 pc, 37 pc, 60 pc, 95 pc, 150 pc and 238 pc respectively. The data set from Region 5 is too small to support wavelet cross correlations of 794'' so correlations are only shown up to 501''. Coverage over the map of CO data is not complete except for Regions 1 and 3.

wavelet correlations extracted from Figure 6 which correlates the Spitzer IR data with the higher resolution 3 cm and 6 cm data, (Dickel *et al.* 2010). The wavelet cross correlation with the Spitzer data shows that the FIR/RC wavelet correlation scale factors extend down to ~ 15 pc. Within each region, all of the FIR bands show similar correlation patterns with RC data with respect to scale factor. The coverage of the regions is quite good for the Spitzer 160 μm data but less so for the Spitzer 70 μm data particularly in Regions 1, 3, and 4. There are also some unexpected differences between the 3 cm and 6 cm correlations with the FIR data.

3.7 Wavelet cross correlation for other bands

H I cross correlation is seen in Figure 5 with 21 cm RC in Region 1. The correlation initially dips before beginning a slow rise to the correlation threshold at ~ 130 pc. Region 2 never achieves correlation threshold and Region 3 doesn't until ~ 170 pc. Regions 4 and 5 have approximately the same scale factor of ~ 85 pc.

$H\alpha$ correlations from Figure 5 in Table 8 with 21 cm RC are essentially at the resolution of the H I data at ~ 25 pc for Regions 1 through 3. Regions 4 and 5 have correlation threshold at larger scale factors of ~ 85 pc. High-resolution $H\alpha$ correlations from Figure 6 in Table 9 with 3 cm and 6 cm shows that the $H\alpha$ wavelet cross correlation extends down to much smaller scale factors from 9 pc to 33 pc for Regions 1 through 4.

The CO correlations are very sparse since the map of the data is rather incomplete. Region 1 had correlation threshold at 97 pc and above. No significant correlation is detected in Region 2. Region 3 had correlation threshold at 229 pc. No other correlations are possible.

4 Discussion

The FIR/RC correlation coefficient, q , determined in this study is very close to the expected value for nor-

Table 9 6 cm and 3 cm RC high resolution wavelet cross correlation scale factors in pc for region 1 through 5 with data from Spitzer and $H\alpha$ data sets. Listed are the minimum scale factors in pc for which the wavelet cross correlations are considered excellent, which is taken to be ≥ 0.75 .

6 cm RC					
Region	1	2	3	4	5
Spitzer 70 μm	43.2	19.8	14.7	23.1	137.3
Spitzer 160 μm	45.2	22.7	17.7	17.6	114.1
$H\alpha$	9.0	14.0	10.4	9.1	87.5
3 cm RC					
Spitzer 70 μm	37.9	27.6	16.4	33.3	129.4
Spitzer 160 μm	39.7	36.8	17.6	35.5	80.6
$H\alpha$	12.6	32.1	17.10	33.8	—

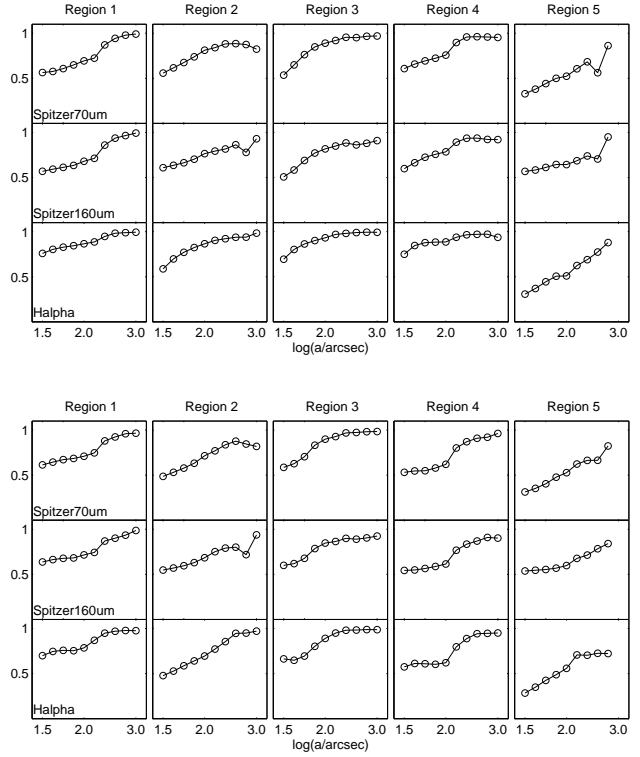


Fig. 6 6 cm (top) and 3 cm (bottom) wavelet cross correlation plots for Regions 1 through 5 with the Spitzer FIR data sets and $H\alpha$ data. These graphs extend the cross correlation calculations down to 9pc. The data points are calculated at scale factors of 31'', 40'', 50'', 63'', 80'', 125'', 200'', 316'', 501'', and 794'' which correspond to 9 pc, 12 pc, 15 pc, 19 pc, 24 pc, 37 pc, 60 pc, 95 pc, 150 pc and 238 pc respectively. Region 5 scale factors are limited to a maximum of 501'', 150 pc due to the small size of the region.

mal galaxies even though the SMC is structurally different from the spiral galaxies which constitute most of the population on which the correlation is based. Spirals generally have a thick underlying non-thermal disk. The expected thermal fraction for the disk of a spiral galaxy is ~ 0.1 (Condon 1992). The three regions that cover the SMC bar measured here all have high thermal ratios of ~ 0.54 to ~ 0.95 (see Figure 7). The existence of the bar, however, is questioned by Zaritsky *et al.* (2000). Their argument centers around the hydrodynamic interaction between gaseous components providing the physical mechanism for the SMC morphology. They further suggest that the SMC is actually spheroidal with highly irregular recent star formation. The overall thermal fraction of the SMC is measured here using 1.4 GHz and 4.8 GHz data to have a value of ~ 0.43 which is higher than previously published values of 0.15-0.40 for the SMC by Loiseau *et al.* (1987) using 1.4 GHz and 2.3 GHz data but lower than the value of 0.71 measured by Israel *et al.* (2010) using 5 GHz and 10 GHz data. However, each of the SMC regions measured here except Region 2 has a thermal fraction of > 0.71 .

The triggers for star formation events in massive spirals are believed to be density waves (Beck 2000). In the SMC, there is not enough mass to support such a mechanism so that the trigger in the SMC is likely to be stochastic which leads to a discontinuous formation history with bursts of star formation lasting short periods of time (Klein and Graeve 1986). With only two SNRs detected in Region 2, there is clearly no evidence of a galactic nucleus with its traditional high star formation rate. Figure 4 shows the distribution of q values in the SMC and there is no indication of the q value decreasing from a "nucleus" to the edge of the galaxy as Helou and Bicay (1993) expect in their "leaky box" FIR/RC model. Figure 4 does show that most of the SMC bar is consistent with q values within Y01's expected limits. The depth of the SMC extends 5-10 kpc along the line of sight, (Martin, Maurice, and Lequeux 1989). The measured thermal fraction leads to the conclusion that there are not enough CRe⁻s to generate higher non-thermal emissions and/or that the magnetic field strength is too low in most regions. The published values of the magnetic field are $5 - 10 \mu\text{G}$ along the bar (Ye and Turtle 1991). Sreekumar and Fichtel (1991) concluded that the cosmic ray energy density level in the SMC is three to five times too low to be in equilibrium with the cosmic ray sources. This low cosmic ray density is described by Klein, Grave, and Beck (1984) to be a result of the internal pressure from the CRe⁻s. This causes rapid diffusion of the CRe⁻s out of the star-forming regions. This is consistent with the observation that the bar has primarily thermal RC emission

in Region 1 and Region 3 where there is high density H I and star formation activity. Region 2 may be populated primarily with CRe⁻s which have diffused out of the two star-forming regions in Region 1 and Region 3.

4.1 FIR/RC Correlation Models

The FIR/RC correlation models examined here start with the assumption that the source of relativistic electrons and ionizing photons is the supernova rate. UV photons from massive stars are absorbed by dust which re-emit the energy in the FIR. The relativistic electrons from the SNRs interact with magnetic fields or interact with ionized gas to produce RC radiation.

Voelk (1989) proposed a calorimeter theory which assumes that all of the ionizing photons are absorbed by dust and all of the energy of the CRe⁻s are dissipated by RC emission within the galaxy. This does not appear to be consistent with the SMC since Sreekumar and Fichtel (1991) determined that most of the CRe⁻s escape the SMC.

Applying the "leaky box" model of Helou and Bicay (1993) most of the ionizing photons and CRe⁻s would escape the SMC. The observational prediction of the model is that q decreases radially from the center of the galaxy to the edges of the galaxy. Regions 1 and 3 are the main star-forming regions in the SMC at the present time. Star formation in Region 2 must be suppressed since the H_2 content is the lowest of any region except for Region 5, see Table 3. Due to the irregular nature of the SMC, different position angles from these star-forming areas point towards very different environments as seen in Figure 4. This does not appear to match the gradual decrease in q modeled by Helou and Bicay particularly since neither a nucleus nor a disk can be identified in the SMC.

Hoernes, Berkhuijsen, and Xu (1998) (referred to hereafter as H01) published a model which decomposes both the RC emission and FIR emission into two parts. M31 is used as their test case. H01 selection of M31 relied on four criteria:

1. M31 is close to the Galaxy and well resolved in both radio and in the FIR.
2. The radio emission is dominated by the non-thermal component.
3. The FIR is dominated by cool dust emission.
4. M31 has a low star formation rate of about an order of magnitude below the Galaxy.

Of these criteria, the SMC is also close enough for well resolved FIR and RC measurements. But the SMC is not dominated by the non-thermal RC component with the overall SMC non-thermal emission at 57% and

a minimum non-thermal emission of only 5% in Region 3, see Figure 7.

The supernova rate (R_s) for the SMC is about 1/350 years, $R_{\text{SMC}} = 2.8 \cdot 10^{-3} \text{SN} \cdot \text{yr}^{-1}$ (Filipovic *et al.* 1998) whereas the Galaxy has a supernova rate of about 1/50 years, $R_{\text{Galaxy}} = 20 \cdot 10^{-3} \text{SN} \cdot \text{yr}^{-1}$ (Diehl *et al.* 2006). Dividing these rates by the galaxies' respective volumes shows that the supernova rate per unit volume is higher in the SMC than in the Galaxy:

$$\frac{R_{\text{SMC}}}{V_{\text{SMC}}} \approx \frac{2.8 \cdot 10^{-3} \text{SN} \cdot \text{yr}^{-1}}{15 \text{kpc}^3} \approx 0.19 \frac{\text{SN}}{\text{kpc}^3 \text{kyr}} \quad (11)$$

$$\frac{R_{\text{Galaxy}}}{V_{\text{Galaxy}}} \approx \frac{20 \cdot 10^{-3} \text{SN} \cdot \text{yr}^{-1}}{1200 \text{kpc}^3} \approx 0.017 \frac{\text{SN}}{\text{kpc}^3 \text{kyr}} \quad (12)$$

Whereas M31 has a star formation rate of an order of magnitude below the Galaxy with those two galaxies approximately the same volume, the SMC has a volumetric supernova rate an order of magnitude above the Galaxy or two orders of magnitude above M31.

The SMC does not appear to be consistent with the criteria needed to apply H01's decomposition model.

4.2 Decomposition of the SMC RC into thermal and non-thermal emission

Data from the Parkes single dish telescope are used for the RC thermal fraction calculations (Filipovic *et al.* 1997) due to its superior overall flux-density accuracy. The Parkes data were converted to a data map with 5'' resolution using the Miriad regrid program to match the 6 cm data set. The thermal fraction of the emissions at 21 cm are calculated using equation 13 from Niklas, Klein, and Wielebinski (1997). $S_{6\text{cm}}$ and $S_{21\text{cm}}$ are the measured flux densities of the regions.

$$\frac{S_{6\text{cm}}}{S_{21\text{cm}}} = f_{th} \left(\frac{\nu_{6\text{cm}}}{\nu_{21\text{cm}}} \right)^{-\alpha_{th}} + f_{nth} \left(\frac{\nu_{6\text{cm}}}{\nu_{21\text{cm}}} \right)^{-\alpha_{nth}} \quad (13)$$

In equation 13, f_{th} is the thermal fraction, f_{nth} is the non-thermal fraction, $f_{nth} = (1 - f_{th})$. The thermal spectral index used is $\alpha_{th} = 0.1$. The non-thermal spectral index is assigned a value of $\alpha_{nth} = 1.09$ after Bot *et al.* (2010). The thermal fractions calculated are 0.81, 0.54, 0.95, 0.84, and 0.76 for Regions 1 through 5 and 0.43 for the SMC, see Figure 7. The thermal fraction calculation assumes that the synchrotron emission spectrum can be described by a single power law and that the ISM is optically thin. This assumption can introduce a bias into the calculated thermal fraction if the spectral index is not constant. The index is

expected to steepen in locations that are increasingly remote from the area where the CRe⁻s were initially accelerated since the energy loss of CRe⁻s is $\sim E^2$. Conversely, in star-forming regions the thermal fraction will likely be overestimated as the spectral index is flatter than in other regions. However, the entire SMC as well as each region shows approximately 4 to 9 times the expected thermal fraction of 0.1 (Condon 1992) which suggests that CRe⁻s are not necessarily the source of the RC energy that makes the FIR/RC correlation so consistent.

4.3 Regional Decomposition of the SMC

The top panel of Figure 7 shows the relationship of the slope of the Weighted Least Squares Fit (WLS) of 21 cm RC verses 60 μm emissions from Table 7 plotted against the estimated thermal fractions. The regions show a strong tendency towards increasing WLS slope with increasing thermal fraction.

Region 3 has the highest WLS slope, the highest thermal fraction, and the highest 21 cm flux density of the five regions. It also has the best Pearson correlation, Table 6, of any region for RC 21 cm with all of the IR data sets, excellent Pearson correlation of 13 cm RC with the higher temperature IR emissions of 60 μm and 70 μm and excellent Pearson correlation of H α with RC 21 cm, 13 cm, IR 60 μm , 70 μm and 160 μm covering cold dust to warm dust emitters. The locations of the high H I concentration correlates with the IR emissions by way of the high Pearson correlation indicating that the H I and dust are co-located. It has excellent wavelet cross correlation of the 21 cm with 60 μm down to the resolution limit of 35 pc. Figure 6 shows the wavelet cross correlation of the higher resolution FIR and RC data (70 μm and 160 μm Spitzer data with 6 cm and 3 cm RC data), indicating that the correlation extends down to 15pc. This region includes N 66 and NGC 346 which is an H II region with embedded stellar association (Bica and Dutra 2000) and the strongest star-forming region in the SMC (Cignoni *et al.* 2011) with 12 SNRs identified.

The next two regions in terms of WLS slope and thermal fraction are Regions 1 and 4. They have WLS slope values and thermal fractions very similar to each other with WLS slope values, ~ 0.85 , and thermal fractions, ~ 0.82 . Region 1 contains N 19 and NGC 267, and Region 4 contains NGC 456 which are H II regions with embedded stellar associations (Bica and Dutra 2000). Region 1 has nine SNRs and high Pearson correlation values for H I with 60 μm , 100 μm , and 160 μm . The excellent wavelet cross correlation of the 21 cm

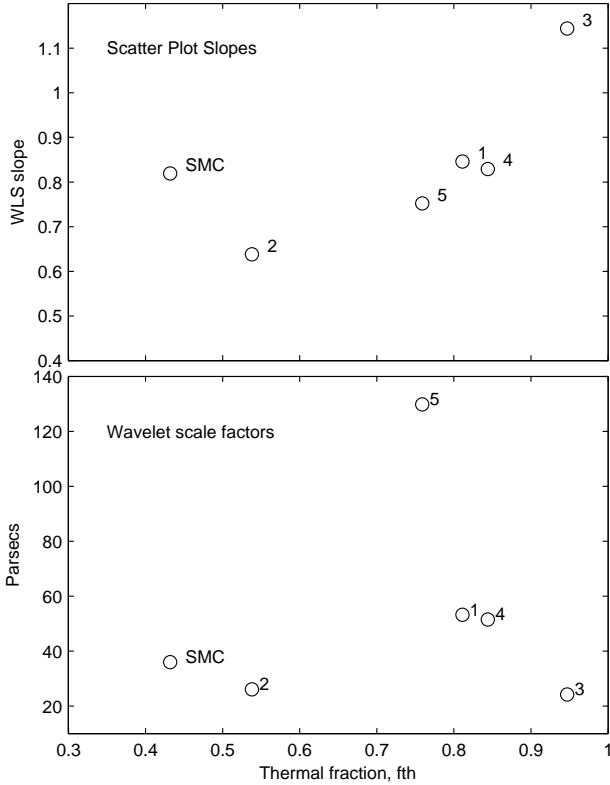


Fig. 7 Top Panel: WLS slope of 21 cm RC versus $60\ \mu\text{m}$ data plotted against the thermal fraction. The thermal fractions plotted are 0.81, 0.54, 0.95, 0.84, and 0.76 for Regions 1 through 5. The SMC estimate is 0.43. Second Panel: Minimum wavelet cross correlation scale factor for 21 cm RC with $60\ \mu\text{m}$ that had excellent correlation. For Regions 1 through 5, those scale factors are 53.2 pc, 28.3 pc, 24.0 pc, 51.5 pc, and 129.8 pc. The Region 2 and 3 are from the higher resolution Spitzer $70\ \mu\text{m}$ data. For the $3^\circ \times 3^\circ$ central portion of the SMC, excellent wavelet correlation is seen down to a scale factor of 36 pc.

RC with $60\ \mu\text{m}$ extends down to 50 pc. Region 4 has excellent Pearson correlation of CO with IR emissions at $60\ \mu\text{m}$, $100\ \mu\text{m}$ and $160\ \mu\text{m}$ with the correlation increasing as the temperature of the dust emission decreases. Interestingly, the 21 cm flux for Region 1 is only slightly below Region 3 but Region 4 has the second lowest flux at about 1/2 of the flux of Region 1. The CO data in Region 4 contains NGC 456 but much of the remainder of the region is not covered in the CO data.

Region 5 has a WLS slope of 0.72 and a thermal fraction of 0.76. The region contains the open cluster NGC 419 which has been examined by Rubele, Kerber, and Girardi (2010) who suggests that the star formation history of the cluster displays continuous star formation over 1.2 to 1.9 Gyr. This region exhibits no strong Pearson correlations in any data set pairs investigated here (Table 6). There is excellent wavelet correlation down to 130 pc which is the largest measured by this study of the SMC. Oddly, the Spitzer $70\ \mu\text{m}$ wavelet correlation with 6 cm RC gives a much smaller correlation threshold, 50 pc, but the Spitzer $70\ \mu\text{m}$ is consistent with the $60\ \mu\text{m}$ correlation threshold when correlated to 6 cm and 3 cm RC data.

Region 2 has the smallest WLS slope of the regions with a value of 0.62. It also displays the smallest thermal fraction of 0.54. It contains NGC 330 which is an open cluster and two SNRs. It contains no strong Pearson correlations. The wavelet correlation threshold is at the resolution limit of 35 pc. The higher resolution wavelet correlation graphs, Figure 6, show the correlation actually goes down to 19 pc.

The thermal fraction of the SMC is estimated here to be 0.43. This is higher than the typical value of ~ 0.1 given by Condon (1992) for spiral galaxies. It is very close to the value of 0.45 for the LMC measured by Hughes *et al.* (2006). The average value of the thermal fraction of the 5 regions is 0.78 over an area of $2.9\ \text{deg}^2$ whereas the SMC measurement is over $9\ \text{deg}^2$. This suggests that the regions, primarily in the bar, emit mostly thermal RC energy but that the larger area contains significant non-thermal emission from a large population of CRe^- s that have diffused out of the bar. The star formation activity is in the bar where the H I has high density. The non-thermal emission is taking place where the H I has low density outside of the bar. The small size of the SMC suggests that the cosmic ray leakage into the nearby areas would be substantial. The total 21 cm flux from the regions is 26.5 Jy and the total flux in the $3^\circ \times 3^\circ$ data set used for these thermal fraction calculations is 36 Jy.

It is interesting to note that the q values that are calculated including only the thermal portion of the

RC emission satisfies Y01's range of q values for normal galaxies for the five regions: 1) 2.90, 2) 2.85, 3) 2.72, 4) 2.83, 5) 2.85. The "greater" SMC has a q value of 3.02 which is just at the 98% q value consistent with Y01's correlation study.

5 Conclusions

We show in this study that the FIR/RC correlations for the SMC and for each of the five regions defined here, are consistent with Y01's regression from 1750 galaxies. The study presented here considers the "greater" SMC and the sub-regions of the bar and wing as well.

Pearson correlation coefficients of RC 21 cm emissions with 60 μm and 100 μm emissions have positive correlation only in Region 3 which is the region with the highest star formation rate. Not surprisingly, Region 3 also has positive Pearson correlation of $H\alpha$ with RC and FIR emissions. Interestingly, Region 1 has twice as much H I and H_2 as Region 3 and has the second highest star formation rate in the SMC. Its strongest Pearson correlations are in terms of H I with FIR emissions. Since the star formation rate in the SMC is predicted to be stochastic, Region 1 may have a suppressed supernova rate at this time.

Pixel by pixel scatter plots indicate two populations of correlations in terms of 21 cm RC and 60 μm emissions. The highest slope is from Region 3 which also has the largest difference between the WLS and OLS slope values, 1.14-0.98, 14.5%. Region 1 has the second largest slope and the second largest difference of slopes of 0.85-0.73, 13.7%. This correlates to the regions with the strongest star formation rate having the strongest indication of two distinct emission populations. The other regions and the SMC have smaller slopes and less significant differences of 7.8% to 3.6%.

The wavelet cross correlation scale factors for the FIR with the RC for the regions are all within 20 to 60 pc except for Region 5 which is ≈ 130 pc and may have few features at small scale factors. There is no clear trend displayed in this correlation. It is interesting to note that the region with the highest thermal fraction, Region 3, and the region with the lowest thermal fraction, Region 2, have the the smallest wavelet correlation scale factors. $H\alpha$ has wavelet cross correlation scale factors with the 6 cm RC emission of between 9 and 14 pc for all of the regions except for Region 5 which is 87 pc.

The regions have q values of: 1) 2.80, 2) 2.58, 3) 2.70, 4) 2.75, 5) 2.73. The measured value of q for the SMC is 2.65 which includes portions of the greater SMC that are not included in regions comprising the bar and wing.

The SMC and all of the regions have q values above Y01's correlation value of 2.34 but well within the values of 1.64 to 3.04 between which 98% of the q values for the galaxies measured by Y01 were found. This suggests that the RC emission in the SMC is slightly deficient compared to the FIR emission. It could be due to CRe^- s escaping the bar or wing of the SMC without losing much of their energy. Since the non-thermal fraction of the RC emission is so small, the non-thermal RC emission is significantly under-luminous considering that the non-thermal fraction is expected to be dominant. This may be due to the small physical size of the SMC and a low magnetic field density.

The SMC displays a thermal fraction that is much higher than is common for disk galaxies. Disk galaxies typically have a thermal fraction of 0.1 (Condon 1992) while the SMC is measured here to have a value of 0.43. The regions have even higher measured values of the thermal fraction, 1) 0.81, 2) 0.54, 3) 0.95, 4) 0.84, and 5) 0.76. This suggests that galaxies can have most of their RC radiation derived from thermal sources powered by the radiation field from high mass stars in H II regions rather than by SNRs. There appears to be a weak correlation between the thermal fraction and the q values. The thermal fraction values above 0.5 correspond to q values above 2.7 and thermal fraction values below about 0.5 have q values of below 2.7. The SMC and all five of the defined regions have FIR/RC correlations consistent with Y01 q values when considering only thermal RC radiation. Thermal radiation can be the major source of RC emission from a galaxy suggesting that measurements of the RC emission of galaxies could lead to over estimating the super nova rate by assuming the 0.1 ratio of thermal to non thermal radiation.

Acknowledgements

We would like to thank the anonymous referee for a careful reading this paper and for the astute comments that improved the final version of this paper significantly.

References

- Appleton, P.N., Fadda, D.T., Marleau, F.R., Frayer, D.T., Helou, G., Condon, J.J., Choi, P.I., Yan, L., Lacy, M., Wilson, G., Armus, L., Chapman, S.C., Fang, F., Heinrichson, I., Im, M., Jannuzi, B.T., Storrie-Lombardi, L.J., Shupe, D., Soifer, B.T., Squires, G., Teplitz, H.I.: *The Astrophysical Journal Supplement Series* **154**, 147 (2004)
- Beck, R.: *Philosophical Transactions: Mathematical, Physical and Engineering Sciences* **358**(1767), 777 (2000). Hand generated referenc.
- Bica, E., Dutra, C.M.: *The Astronomical Journal* **119**, 1214 (2000)
- Blackburn, J.K., Payne, H.E., Hayes, J.J.E.: 1995 Ftools: A fits data processing and analysis software package
- Bolatto, A.D., Simon, J.D., Stanimirovic, S., van Loon, J.T., Shah, R.Y., Venn, K., Leroy, A.K., Sandstrom, K., Jackson, J.M., Israel, F.P., Li, A., Staveley-Smith, L., Bot, C., Boulanger, F., Rubio, M.: *The Astrophysical Journal* **655**, 212 (2007)
- Bot, C., Ysard, N., Paradis, D., Bernard, J.P., Lagache, G., Israel, F.P., Wall, W.F.: *Astronomy and Astrophysics* **523**, 20 (2010)
- Cignoni, M., Tosi, M., Sabbi, E., Nota, A., Gallagher, J.S.: *The Astronomical Journal* **141**, 31 (2011)
- Cioni, M.R.L., Habing, H.J., Israel, F.P.: *Astronomy and Astrophysics* **358**, 9 (2000)
- Condon, J.J.: *Annual Review of Astronomy and Astrophysics* **30**, 575 (1992)
- Costa, E., Mndez, R.A., Pedreros, M.H., Moyano, M., Gallart, C., Nol, N.: *The Astronomical Journal* **141**, 136 (2011)
- Crawford, E.J., Filipovic, M.D., De Horta, A.Y., Wong, G.F., Tothill, N.F.H., Draskovic, D., Collier, J.D., Galvin, T.J.: 2011 New 6 and 3-cm radio-continuum maps of the small magellanic cloud. part i - the maps. 10 Pages, 6 figures, accepted for publication in the *Serbian Astronomical Journal*
- Dickel, J.R., Gruendl, R.A., McIntyre, V.J., Amy, S.W.: *The Astronomical Journal* **140**, 1511 (2010)
- Diehl, R., Halloin, H., Kretschmer, K., Lichti, G.G., Schnfelder, V., Strong, A.W., von Kienlin, A., Wang, W., Jean, P., Knudseder, J., Roques, J.P., Weidenspointner, G., Schanne, S., Hartmann, D.H., Winkler, C., Wunderer, C.: *Nature* **439**, 45 (2006)
- Filipovic, M.D., Haynes, R.F., White, G.L., Jones, P.A., Klein, U., Wielebinski, R.: *Astronomy and Astrophysics Supplement Series* **111**, 311 (1995)
- Filipovic, M.D., Jones, P.A., White, G.L., Haynes, R.F., Klein, U., Wielebinski, R.: *Astronomy and Astrophysics Supplement Series* **121**, 321 (1997)
- Filipovic, M.D., Haynes, R.F., White, G.L., Jones, P.A.: *Astronomy and Astrophysics Supplement Series* **130**, 421 (1998)
- Filipovic, M.D., Jones, P.A., White, G.L., Haynes, R.F.: *Astronomy and Astrophysics Supplement Series* **130**, 441 (1998a)
- Filipovic, M.D., Pietsch, W., Haynes, R.F., White, G.L., Jones, P.A., Wielebinski, R., Klein, U., Dennerl, K., Kahabka, P., Lazendic, J.S.: *Astronomy and Astrophysics Supplement Series* **127**, 119 (1998b)
- Filipovic, M.D., Bohlson, T., Reid, W., Staveley-Smith, L., Jones, P.A., Nohejl, K., Goldstein, G.: *Monthly Notices of the Royal Astronomical Society* **335**, 1085 (2002). DOI: 10.1046/j.1365-8711.2002.05702.x
- Filipovic, M.D., Payne, J.L., Reid, W., Danforth, C.W., Staveley-Smith, L., Jones, P.A., White, G.L.: *Monthly Notices of the Royal Astronomical Society* **364**, 217 (2005). DOI: 10.1111/j.1365-2966.2005.09554.x
- Frick, P., Beck, R., Berkhuijsen, E.M., Patrickeyev, I.: *Monthly Notices of the Royal Astronomical Society* **327**, 1145 (2001). DOI: 10.1046/j.1365-8711.2001.04812.x; eprintid: arXiv:astro-ph/0109017
- Gooch, R., Barnes, J.: 1996 Karma: a visualization test-bed
- Haslam, C.G.T., Osborne, J.L.: *Nature* **327**, 211 (1987)
- Haynes, R.F., Klein, U., Wayte, S.R., Wielebinski, R., Murray, J.D., Bajaja, E., Meinert, D., Buczylowski, U.R., Harnett, J.I., Hunt, A.J., Wark, R., Sciacca, L.: *Astronomy and Astrophysics* **252**, 475 (1991)
- Helder, E.A., Vink, J., Bassa, C.G., Bamba, A., Bleeker, J.A.M., Funk, S., Ghavamian, P., van der Heyden, K.J., Verbunt, F., Yamazaki, R.: *Science* **325**, 719 (2009). DOI: 10.1126/science.1173383; eprintid: arXiv:0906.4553
- Helou, G., Bica, M.D.: *Astrophysical Journal* **415**, 93 (1993)
- Helou, G., Khan, I.R., Malek, L., Boehmer, L.: *Astrophysical Journal Supplement Series* **68**, 151 (1988)
- Hilditch, R.W., Howarth, I.D., Harries, T.J.: *Monthly Notices of the Royal Astronomical Society* **357**, 304 (2005)
- Hoernes, P., Berkhuijsen, E.M., Xu, C.: *Astronomy and Astrophysics* **334**, 57 (1998)
- Hughes, A., Wong, T., Ekers, R., Staveley-Smith, L., Filipovic, M., Maddison, S., Fukui, Y., Mizuno, N.: *Monthly Notices of the Royal Astronomical Society* **370**, 363 (2006)
- Israel, F.P., Wall, W.F., Raban, D., Reach, W.T., Bot, C., Oonk, J.B.R., Ysard, N., Bernard, J.P.: *Astronomy and Astrophysics* **519**, 67 (2010)
- Joye, W.A., Mandel, E., Jedrzejewski, R.I., Hook, R.N.: 2003 New features of saomage ds9
- Klein, U., Graeve, R.: *Astronomy and Astrophysics* **161**, 155 (1986)
- Klein, U., Grave, R., Beck, R.: 1984 Radio continuum emission from magellanic-type and dwarf irregular galaxies
- Klein, U., Haynes, R.F., Wielebinski, R., Meinert, D.: *Astronomy and Astrophysics* **271**, 402 (1993)
- Koornneef, J., de Boer, K.S.D.: 1984 Gas-to-dust ratios in the magellanic clouds
- Leroy, A.K., Bolatto, A., Gordon, K., Sandstrom, K., Gratier, P., Rosolowsky, E., Engelbracht, C.W., Mizuno, N., Corbelli, E., Fukui, Y., Kawamura, A.: *The Astrophysical Journal* **737**, 12 (2011)
- Leroy, A., Bolatto, A., Stanimirovic, S., Mizuno, N., Israel, F., Bot, C.: *Astrophysical Journal* **658**, 1027 (2007). DOI: 10.1086/511150; eprintid: arXiv:astro-ph/0611687
- Loiseau, N., Klein, U., Greybe, A., Wielebinski, R., Haynes, R.F.: *Astronomy and Astrophysics* **178**, 62 (1987)
- Maragoudaki, F., Kontizas, M., Morgan, D.H., Kontizas, E., Dapergolas, A., Livanou, E.: *Astronomy and Astrophysics* **379**, 864 (2001)

- Martin, N., Maurice, E., Lequeux, J.: *Astronomy and Astrophysics* **215**, 219 (1989)
- Matlab: 2010 Matlab 7.10.0, The MathWorks Inc.
- Miville-Deschênes, M.A., Lagache, G.: *The Astrophysical Journal Supplement Series* **157**, 302 (2005)
- Mizuno, N., Rubio, M., Mizuno, A., Yamaguchi, R., Onishi, T., Fukui, Y.: *Publications of the Astronomical Society of Japan* **53**, 45 (2001)
- Murai, T., Fujimoto, M.: *Publications of the Astronomical Society of Japan* **32**, 581 (1980)
- Niklas, S., Klein, U., Wielebinski, R.: *Astronomy and Astrophysics* **322**, 19 (1997)
- Payne, J.L., Filipovic, M.D., Reid, W., Jones, P.A., Staveley-Smith, L., White, G.L.: *Monthly Notices of the Royal Astronomical Society* **355**, 44 (2004). DOI: 10.1111/j.1365-2966.2004.08287.x
- Payne, J.L., White, G.L., Filipovic, M.D., Pannuti, T.G.: *Monthly Notices of the Royal Astronomical Society* **376**, 1793 (2007). DOI: 10.1111/j.1365-2966.2007.11561.x
- Piatek, S., Pryor, C., Olszewski, E.W.: *The Astronomical Journal* **135**, 1024 (2008)
- Reid, W.A., Payne, J.L., Filipovic, M.D., Danforth, C.W., Jones, P.A., White, G.L., Staveley-Smith, L.: *Monthly Notices of the Royal Astronomical Society* **367**, 1379 (2006). DOI: 10.1111/j.1365-2966.2006.10017.x
- Rubele, S., Kerber, L., Girardi, L.: *Monthly Notices of the Royal Astronomical Society* **403**, 1156 (2010)
- Sandage, A., Tammann, G.A.: *A revised shapley-ames catalog of bright galaxies*. Carnegie Institution of Washington publication ; 635, p. 157. Carnegie Institution of Washington, Washington, D.C. (1981). Allan Sandage and G.A. Tammann. ill. ; 32 cm.
- Sandage, A., Bedke, J., of Washington., C.I., Foundation., F.: *The carnegie atlas of galaxies*. Carnegie Institution of Washington publication ; 638., p. 2. Carnegie Institution of Washington, with the Flintridge Foundation, Washington, D.C. (1994). by Allan Sandage and John Bedke. chiefly ill. ; 36 x 45 cm. Includes index (v. 2).
- Sault, R.J., Teuben, P.J., Wright, M.C.H.: 1995 *A retrospective view of miriad*
- Schlegel, D.J., Finkbeiner, D.P., Davis, M.: *Astrophysical Journal* **500**, 525 (1998)
- Schure, K.M., Vink, J., Achterberg, A., Keppens, R.: *Advances in Space Research* **44**, 433 (2009). DOI: 10.1016/j.asr.2009.05.010; eprintid: arXiv:0905.1134
- Schwering, P.B.W., Israel, F.P.: *Ir sources in magellanic clouds (schwering+ 1990)*. VizieR Online Data Catalog, vol. 2181, p. 0 (1993). Machine readable data available in Downloads directory
- Smith, C., Leiton, R., Pizarro, S.: In: *Stars, Gas and Dust in Galaxies: Exploring the Links* vol. 221, p. 83. ISBN: jISBN1-58381-053-6j/ISBN1-
- Sreekumar, P., Fichtel, C.E.: *Astronomy and Astrophysics* **251**, 447 (1991)
- Stanimirovic, S., Staveley-Smith, L., Dickey, J.M., Sault, R.J., Snowden, S.L.: *Monthly Notices of the Royal Astronomical Society* **302**, 417 (1999)
- Staveley-Smith, L., Sault, R.J., McConnell, D., Kesteven, M.J., Hatzidimitriou, D., Freeman, K.C., Dopita, M.A.: *Publications of the Astronomical Society of Australia* **12**, 13 (1995)
- Staveley-Smith, L., Sault, R.J., Hatzidimitriou, D., Kesteven, M.J., McConnell, D.: *Monthly Notices of the Royal Astronomical Society* **289**, 225 (1997)
- Voelk, H.J.: *Astronomy and Astrophysics* **218**, 67 (1989)
- Weingartner, J.C., Draine, B.T.: *Astrophysical Journal* **548**, 296 (2001)
- Westerlund, B.E.: *The magellanic clouds*. Cambridge astrophysics series ; 29, p. 279. Cambridge University Press, New York (1997). Bengt E. Westerlund. ill.
- Wong, G.F., Filipovic, M.D., Crawford, E.J., de Horta, A.Y., Galvin, T., Draskovic, D., Payne, J.L.: *Serbian Astronomical Journal* **182**, 43 (2011)
- Wong, G.F., Filipovic, M.D., Crawford, E.J., Tothill, N.F.H., de Horta, A.Y., Draskovic, D., Galvin, T.J., Collier, J.D., Payne, J.L.: *Serbian Astronomical Journal* **183**, 103 (2011a)
- Wong, G.F., Crawford, E.J., Filipovic, M.D., De Horta, A.Y., Tothill, N.F.H., Collier, J.D., Draskovic, D., Galvin, T.J., Payne, J.L.: *ArXiv e-prints* **1203**, 4310 (2012). 25 pages, 2 tables, submitted to SAJ
- Xu, C., Klein, U., Meinert, D., Wielebinski, R., Haynes, R.F.: *Astronomy and Astrophysics* **257**, 47 (1992)
- Ye, T., Turtle, A.J.: *Monthly Notices of the Royal Astronomical Society* **249**, 693 (1991)
- Yun, M.S., Reddy, N.A., Condon, J.J.: *Astrophysical Journal* **554**, 803 (2001)
- Zaritsky, D., Harris, J., Grebel, E.K., Thompson, I.B.: *Astrophysical Journal* **534**, 53 (2000)